



Enhancement of photocatalytic hydrogen evolution activity of porous oxygen doped g-C₃N₄ with nitrogen defects induced by changing electron transition



Yabin Jiang^a, Zongzhao Sun^a, Chao Tang^a, Yuxia Zhou^a, Lei Zeng^{a,b,*}, Limin Huang^{a,*}

^a Department of Chemistry, Southern University of Science and Technology, Shenzhen, Guangdong 518055, China

^b School of Materials Science and Engineering, Nanyang Technological University, 50 Nanyang Avenue, Singapore 639798, Singapore

ARTICLE INFO

Keywords:

Photocatalytic hydrogen evolution
g-C₃N₄
Nitrogen defects
Oxygen doping
Electron transition

ABSTRACT

Porous structure, nitrogen defects and oxygen dopants are simultaneously introduced into the framework of graphitic carbon nitride (g-C₃N₄) by a simple co-pyrolysis of dicyandiamide and ammonium persulphate ((NH₄)₂S₂O₈). The (NH₄)₂S₂O₈ plays multi-function roles in the co-pyrolysis process. It not only restrains polycondensation to generate nitrogen defects but also introduces porous structure and oxygen dopants due to its strong oxidative ability. The synergetic effect of the nitrogen defects and oxygen dopants leads to the change of π band state and LP state (lone pair electrons), causing the change of electron transition in the modified g-C₃N₄. The transitions from impurity levels play a predominant role in excitation process while the transition from intrinsic HOMO to LUMO becomes subordinate, which improve the charge separation significantly. The modified g-C₃N₄ exhibits excellent photocatalytic hydrogen evolution activity under visible light illumination, which is almost 6 times higher than pristine g-C₃N₄ because of the improved efficiency of charge separation and increased specific surface area. These findings provide a simple and efficient method to improve the photocatalytic activity of g-C₃N₄ by changing the electron transition through a rational band structure engineering.

1. Introduction

With the continuous development of the world and the increasing demand for clean and sustainable energy, hydrogen energy as a promising ideal alternative to fossil fuel has been intensively attractive, especially hydrogen evolution from water splitting driven by sun light. Graphitic carbon nitride (g-C₃N₄), a new metal-free polymeric photocatalyst, has stimulated tremendous research attention for hydrogen evolution due to its excellent physiochemical property, such as high thermal and chemical stability, suitable electronic band structure, low-cost and easy preparation [1,2,3,4,5,6]. However, the photocatalytic performance of bulk g-C₃N₄ is still unsatisfactory due to its low electrical conductivity, limited optical absorption and fast photogenerated charge carrier recombination [7,8,9,10]. After years of effort, several strategies have been developed to improve the photocatalytic activity of g-C₃N₄, including the construction of a porous structure [11], element doping [12], modification with carbon material [13], noble metal deposition [14] and coupling with other semiconductors to form hybridized composites [15].

The porous structure provides readily accessible channels for reactant adsorption, and more surface-active sites for reaction [16]. The general method to construct porous structure for catalytic reactions, includes hard-templating and soft-templating methods [17,18]. However, the method generally uses hazardous and environmentally unfriendly chemicals such as ammonium fluoride or hydrogen fluoride to remove the template, and also introduces carbon residue, which is undesirable for photocatalysis. Therefore, it is necessary to develop a simple method to construct structurally porous g-C₃N₄. In addition, it is widely used to introduce nitrogen defects into g-C₃N₄ framework for improving its photocatalytic activity. Niu et al. [19] reported that the introduction of nitrogen vacancy exerted remarkable effects on modifying the electron structure of g-C₃N₄. The intrinsic radiative recombination of charge carriers is greatly restrained. Thus, the nitrogen deficient g-C₃N₄ showed improved photocatalytic activity for hydrogen evolution and decomposition of Rhodamine B under both UV–vis and visible light. Zhang et al. [20] found that the photocatalytic hydrogen evolution rate of g-C₃N₄ with the introduction of two types of nitrogen defects (cyano group and nitrogen vacancy) is 26 times higher than that

* Corresponding author.

** Corresponding author at: School of Materials Science and Engineering, Nanyang Technological University, Singapore, 639798, Singapore.

E-mail addresses: zenglei@ntu.edu.sg (L. Zeng), huanglm@sustc.edu.cn (L. Huang).

<https://doi.org/10.1016/j.apcatb.2018.08.059>

Received 24 April 2018; Received in revised form 10 August 2018; Accepted 23 August 2018

Available online 24 August 2018

0926-3373/© 2018 Elsevier B.V. All rights reserved.

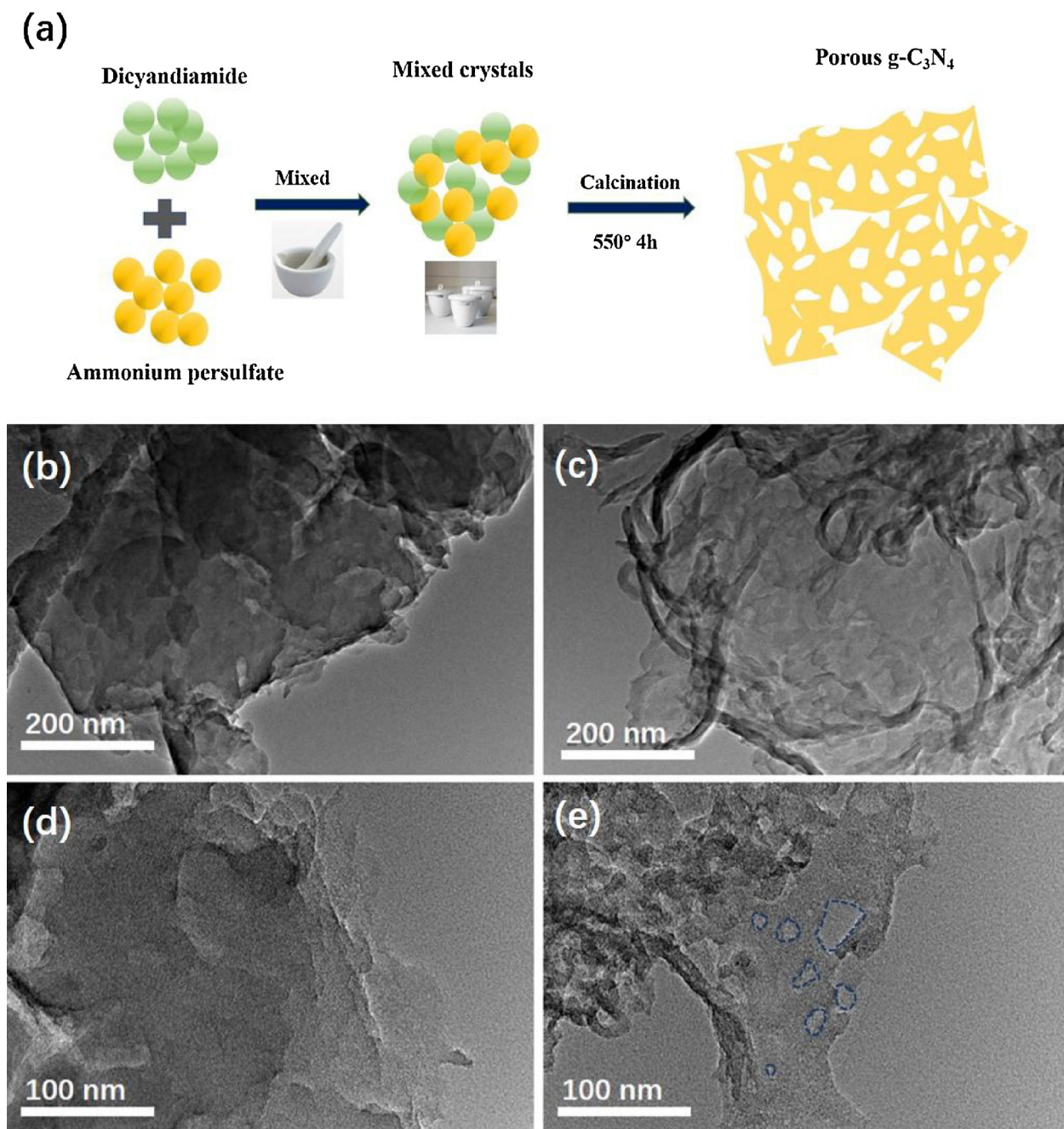


Fig. 1. Schematic illustration for the formation of porous g-C₃N₄ (a). TEM images of bulk g-C₃N₄ (b, d) and p-CN2 (c, e) samples. (For interpretation of the references to colour in the text, the reader is referred to the web version of this article.)

of bulk g-C₃N₄. It was mainly ascribed to the combination effect of porous feature, as-formed defects and increased specific surface area. Yu et al. [21] demonstrated that the band structure of g-C₃N₄ could be adjusted by cyano groups and surface nitrogen vacancies, which are favorable for harvesting visible light and separate photoexcited charge carriers efficiently.

Besides, nonmetal heteroatom (O, S and P) doping is also an effective method to alter the band structure, improve separate rate of charge carriers and expand the range of light absorption for g-C₃N₄ [22,23,24]. Therein, oxygen doping has attracted much attention due to its easy preparation and good performance. Li et al. [25] prepared oxygen-doped g-C₃N₄ for the first time by using a facile H₂O₂ hydrothermal approach which improved the surface area, extended the visible light response of g-C₃N₄, and enhanced the separation efficiency of photo-generated charge carriers. Huang et al. [26] fabricated a porous

oxygen-doped g-C₃N₄ by a facile precursor pre-treatment method, which showed excellent photocatalytic H₂ evolution activity with apparent quantum efficiency of 7.8% at 420 nm. Additionally, Qiu et al. [27] developed a novel metal-free oxygen doped porous graphitic carbon nitride, which displayed a high initial rate of hydrogen evolution (0.098 mmol g_{cat}⁻¹ h⁻¹) due to the increase of specific surface area, the improvement of charge separation rate, and red-shift of light adsorption edge (up to 700 nm). However, to our best knowledge, the combination of nitrogen defects and nonmetal heteroatom doping in the porous g-C₃N₄ has rarely been reported.

The present work reports on a simple one-pot co-pyrolysis method that produces a porous oxygen doped g-C₃N₄ with nitrogen defects (modified g-C₃N₄), which presents 6 times improved photocatalytic activity compared to pristine g-C₃N₄. It is found that (NH₄)₂S₂O₈ plays multiple roles during the thermal polymerization process. More

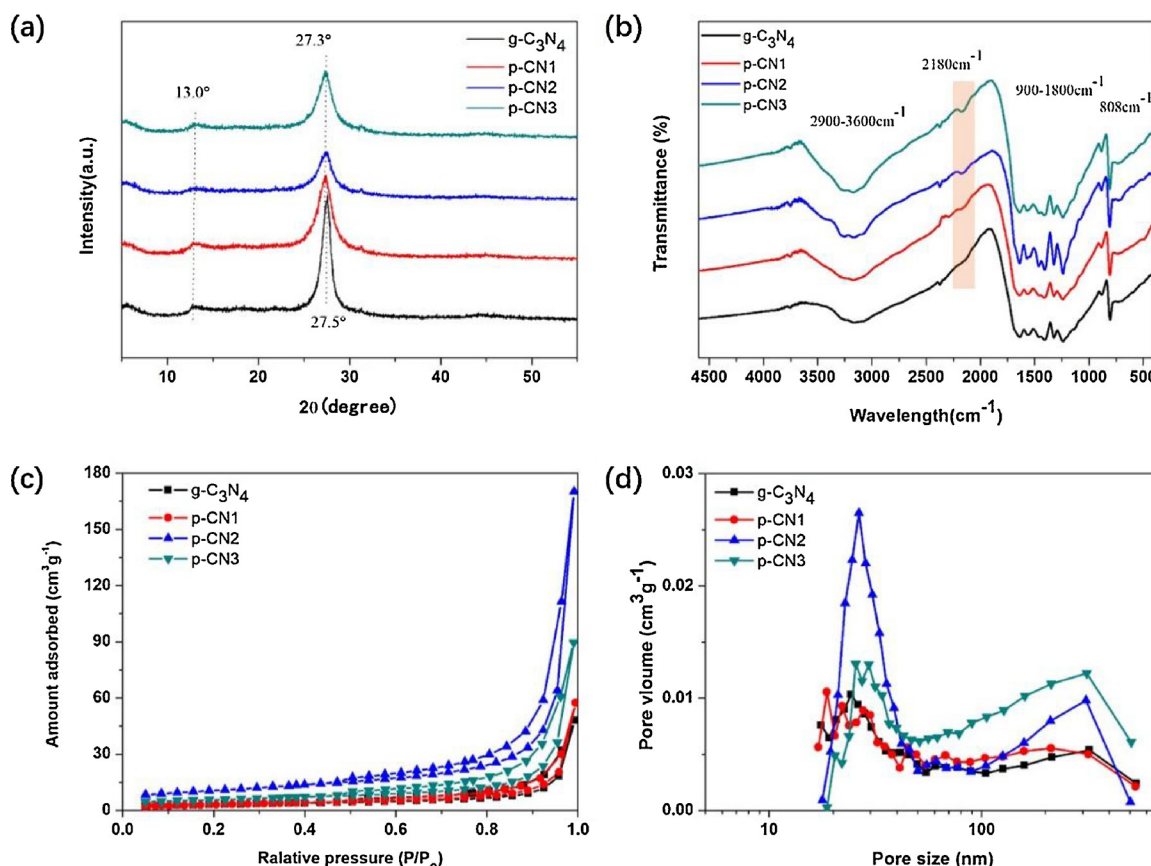


Fig. 2. XRD patterns (a) and FTIR spectra (b) of bulk $g\text{-C}_3\text{N}_4$, p-CN1, p-CN2 and p-CN3 samples. Nitrogen adsorption-desorption isotherms (c) and pore size distribution (d) of bulk $g\text{-C}_3\text{N}_4$, p-CN1, p-CN2 and p-CN3 samples.

importantly, the path of electron transition has been changed by the introduction of nitrogen defects and oxygen dopants, which affects the π band state and LP state in the modified $g\text{-C}_3\text{N}_4$. Thus, the charge separation is improved significantly. The excellent photocatalytic activity of the modified $g\text{-C}_3\text{N}_4$ is ascribed to the increased surface area of porous structure, enhanced light absorption and improved charge separation. Our findings reveal the important role of ammonium persulfate to synthesize modified $g\text{-C}_3\text{N}_4$ and provide a different idea to improve the photocatalytic activity of $g\text{-C}_3\text{N}_4$ by changing electron transition, which is caused by the synergetic effect between nitrogen defects and oxygen dopants.

2. Experimental section

2.1. Materials and reagents

Dicyandiamide was purchased from Aladdin Industrial Corporation. $(\text{NH}_4)_2\text{S}_2\text{O}_8$ was supplied by Tianjin kaitong chemical reagent Co., Ltd, China. Triethanolamine (TEOA) was also provided by Aladdin Industrial Corporation. All reagents used in this study were at least in analytical grade without further purification. Deionized water was used for all experiments.

2.2. Preparation of photocatalysts

The porous $g\text{-C}_3\text{N}_4$ samples were synthesized by a one-step pyrolysis treatment of dicyandiamide and a certain amount of ammonium persulfate. The simple preparation method is as follows: dicyandiamide (2 g) and a certain amount of ammonium persulfate were uniformly mixed and ground thoroughly. Then the powders were put into muffle furnace and heated at 550°C for 4 h with a heating rate of $5^\circ\text{C}/\text{min}$.

When the program was finished, the furnace was cooled to room temperature automatically. The samples with mass ratios of ammonium persulfate to dicyandiamide of 0.25:1, 0.5:1, and 0.75:1 were signed as p-CN1, p-CN2, and p-CN3, respectively. For comparison, a bulk $g\text{-C}_3\text{N}_4$ sample was prepared by the pyrolysis of dicyandiamide without adding ammonium persulfate. Following the synthesis, all products were collected, grounded and washed repeatedly with deionized water, and then dried at 60°C for 10 h.

2.3. Characterization

Powder X-ray diffraction (XRD) measurements were performed on a Rigaku smartlab system at 45 kV and 200 mA with $\text{Cu-K}\alpha$ radiation ($L_{K\alpha1} = 1.540593 \text{ \AA}$, $L_{K\alpha2} = 1.544414 \text{ \AA}$). Data were recorded at a scan rate of 0.02° in 2θ . Fourier transform infrared (FTIR) spectra were recorded on a Bruker VERTEX 70 spectrophotometer, and the samples were prepared as KBr pellets. X-ray photoelectron spectroscopy (XPS) data were obtained on a Thermo ESCALAB250 instrument with a monochromatized $\text{Al K}\alpha$ line source (200 W). The shift of binding energy due to relative surface charging was corrected using the C 1s level at 284.6 eV as an internal standard. The spectra were fitted using a nonlinear least square fitting program (XPSPEAK) with a Shirley background and to the 80% Gaussian/20% Lorentzian peak shape. Nitrogen adsorption-desorption isotherms were collected at a Micromeritics ASAP 2020 surface area and porosity analyzer. The sample was degassed at 413 K for 5 h and then analyzed at 77 K . The relative pressure (P/P_0) range used for calculation of BET surface area was from 0.05 to 0.35. The scanning emission microscope (SEM) measurements were conducted using a FEI Nova Nano SEM 230 Field Emission Scanning Electron Microscope. Transmission electron microscopy (TEM) image was recorded using a FEI Tecnai F30 at an

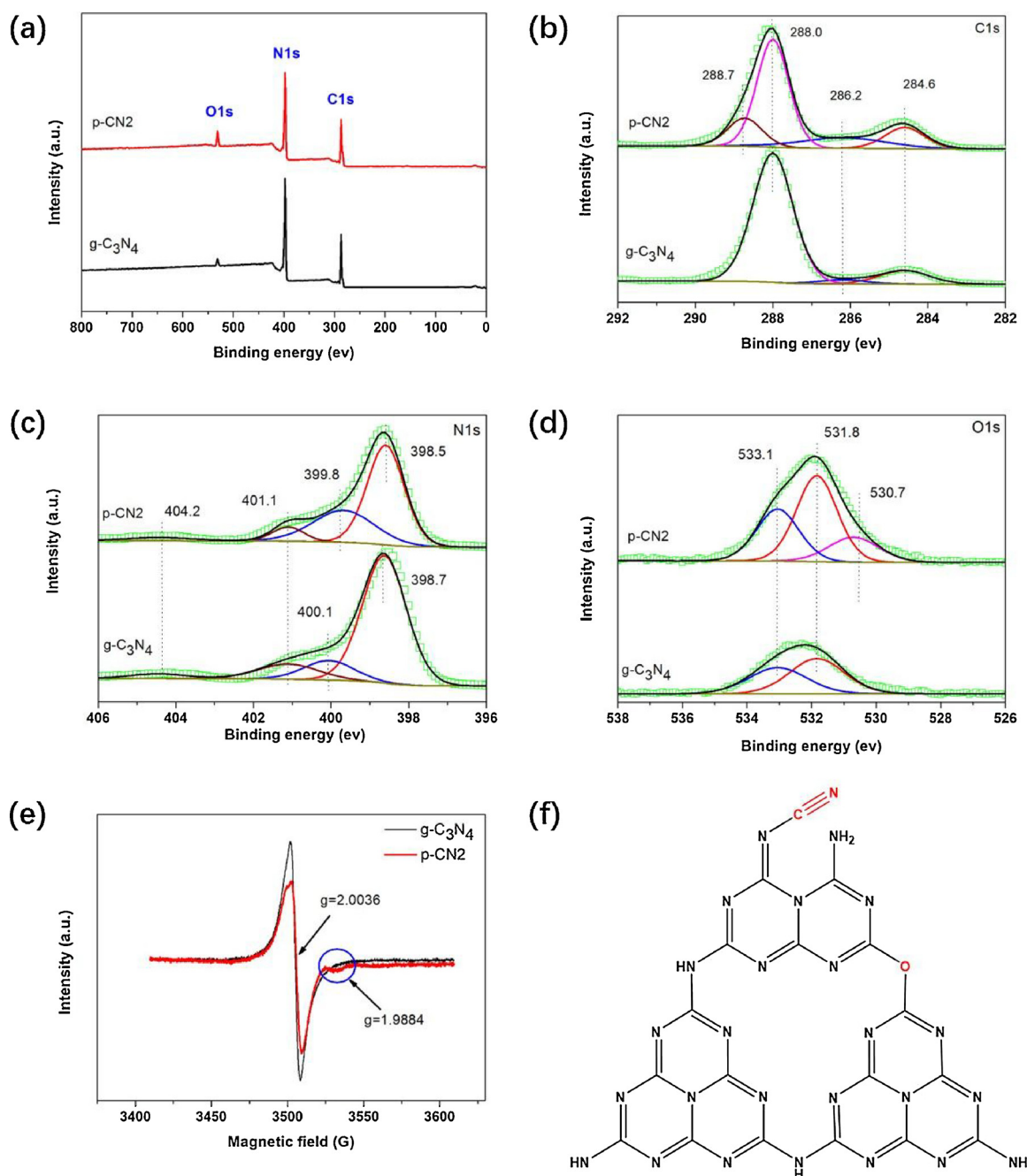


Fig. 3. XPS survey spectra (a), High-resolution C 1s spectra (b), N 1s spectra (c) and O 1s spectra (d) of bulk g-C₃N₄ and p-CN2 samples. Room-temperature EPR spectra for bulk g-C₃N₄ and p-CN2 samples (e), and the diagram of N-defected and O-doped tri-s-triazine unit in p-CN2 (f).

accelerating voltage of 300 kV. UV–vis diffuse reflectance spectra (DRS) were performed on a UV–vis spectrophotometer (Lambda 900, PerkinElmer, USA). BaSO₄ was used as a reflectance standard. The optical properties were evaluated by F(R), and they were applied with a Kubelka–Munk correction. Photoluminescence spectra were recorded on a LabRAM HR spectrometer (HORIBA Jobin Yvon, France) under the excitation wavelength of 325 nm at room temperature. Electron paramagnetic resonance (EPR) measurements were carried out on a Bruker model A300 spectrometer. The settings for the EPR spectrometer were as follows: center field, 3510.00 G; microwave frequency, 9.79 GHz; power, 5.05 mW. The steady-state photoluminescence spectra were gained by using LabRAM HR spectrometer (HORIBA Jobin Yvon, France) with a laser excitation of 325 nm.

2.4. Photocatalytic H₂ evolution

The photocatalytic H₂ production experiments were performed in an online photocatalytic hydrogen production system (CEL-SPH2N, CEALIGHT, Beijing). In a typical experiment, 50 mg of photocatalyst powder was suspended in 50 mL aqueous solution (40 mL 3 wt.% H₂PtCl₆·6H₂O solution and 10 mL triethanolamine). Then, the solution was degassed and irradiated by a 300 W Xenon lamp (CEALIGHT CEL-HXF300, Beijing) with a UV cut-off filter ($\lambda > 420$ nm). The photocatalytic hydrogen evolution rate was quantified by using an online gas chromatograph (GC D7860, TCD detector, N₂ carrier, 5A molecular sieve column, Shanghai Jinghe Chromatograph Co., Ltd). Moreover, by using the similar procedure as above, 50 mg of photocatalyst was used for the apparent quantum yield (AQY) measurement under the

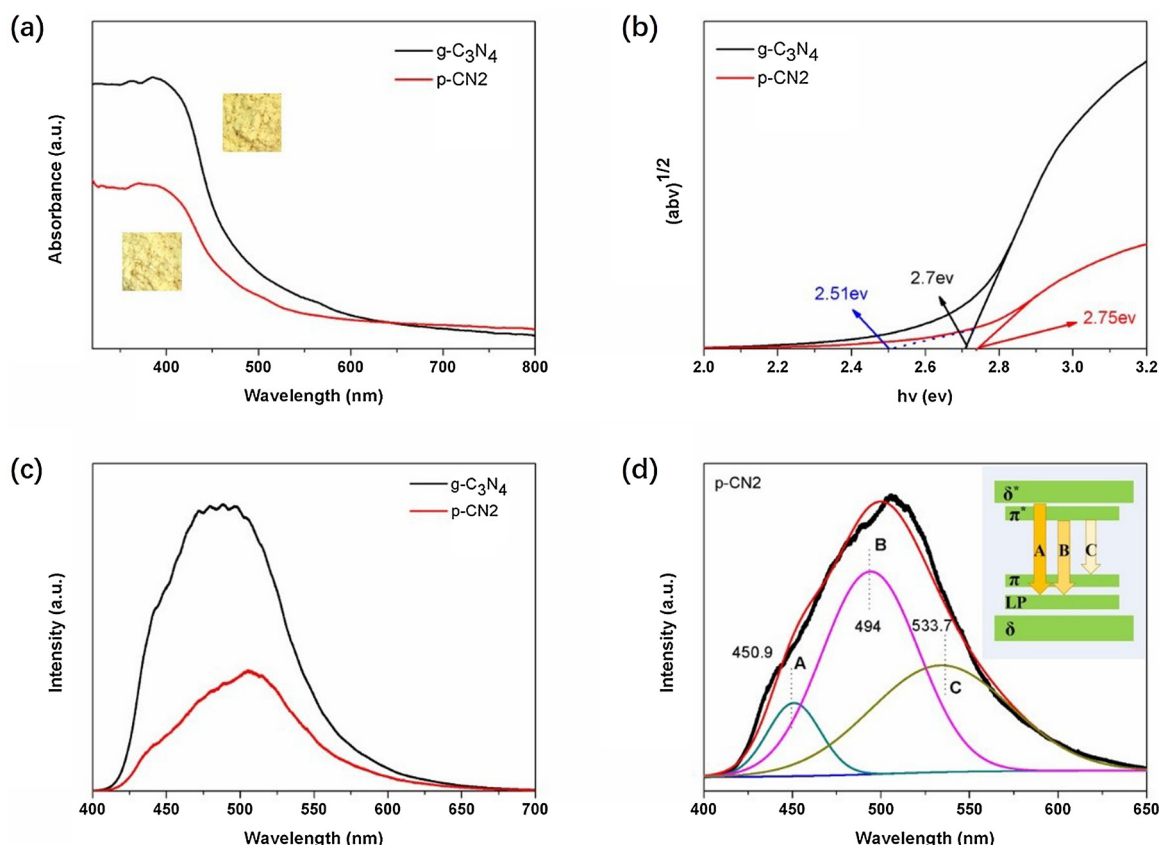


Fig. 4. UV-vis DRS spectra (a) and the bandgaps (b) of bulk g-C₃N₄ and p-CN2 samples, PL spectra (excitation wavelength: 380 nm) of bulk g-C₃N₄ and p-CN2 samples (c), and PL spectra deconvoluted into three Gaussian peaks at approximately (A) 450.9, (B) 494, and (C) 533.7 nm for p-CN2 (d). Inset of (d) shows the photoluminescence emission peaks A, B, and C, which indicate the electron transition from δ^* to LP, π^* to LP, and π^* to π states in a PL system, respectively. (For interpretation of the references to colour in the text, the reader is referred to the web version of this article.)

wavelengths of 420, 450, 500 and 600 nm band-pass filters, respectively. The AQY was calculated by the following equation:

$$\text{AQY (\%)} = 2 \times \text{number of evolved H}_2 \text{ molecules} \times 100 / \text{number of incident photons}$$

2.5. Photoelectrochemical measurements

Electrochemical measurements were conducted with a BAS Epsilon Electrochemical System in a conventional three electrode cell, using a Pt plate as the counter electrode and an Ag/AgCl electrode (3 M KCl) as the reference electrode, the active area is confined to 0.25 cm². The electrolyte was 0.1 M Na₂SO₄ aqueous solution without additive (pH 6.9). The working electrode was prepared on indium-tin oxide (ITO) glass that was cleaned by sonication in ethanol for 30 min and dried at 353 K. The boundary of ITO glass was protected using Scotch tape. The 5 mg sample was dispersed in 1 mL of solution containing 980 μ L absolute ethanol of and 20 μ L of Nafion solution, and the mixed solution was under ultrasonication for 30 min to get a slurry. The slurry was spread onto pretreated ITO glass. After air-drying, the working electrode was further dried at 373 K for 2 h to improve adhesion. Then, the Scotch tape was unstuck, and the uncoated part of the electrode was isolated with epoxy resin. The transient photocurrent was obtained by using a 30 s on-off light cycle at a bias voltage of 0.2 V. Electrochemical impedance spectra were collected in the frequency range from 0.01–10⁶ Hz with a 5 mV sinusoidal AC voltage. The Mott-Schottky plots were measured at the frequency of 1000 Hz. The visible light source came from a 300 W Xe lamp with a filter ($\lambda > 420$ nm).

3. Result and discussion

3.1. Structural properties of as-prepared samples

Fig. 1a shows the synthesis process of modified g-C₃N₄. The detailed synthesis procedure is described in experimental section. The morphologies of bulk g-C₃N₄ and p-CN2 were studied by scanning electron microscopy (SEM) and transmission electron microscopy (TEM), as shown in Figs. S1 and 1b–e. From the SEM images in Fig. S1A, dense and thick layers could be observed in g-C₃N₄, which would suppress its capabilities of light absorption, charge and mass transport [28]. After (NH₄)₂S₂O₈ treatment, the p-CN2 exhibits a loose and porous morphology, as shown in Fig. S1B. In Fig. 1b and d, it is clearly that large sized and overlapped nanosheets can be seen in the TEM image for bulk g-C₃N₄. After the modification of (NH₄)₂S₂O₈, the size of nanosheets is reduced and some pores are clearly presented in p-CN2 (Fig. 1e, marked by blue dash circle). Compared with g-C₃N₄, p-CN2 appears much brighter in the TEM image, indicating that its thickness is thinner.

As shown in Fig. 2a, a similar crystalline structure is detected for both bulk g-C₃N₄ and p-CN2. The main diffraction peaks are observed at around 13.0° and 27.5°, corresponding to the in-planar structurally repeated motifs of triazine rings and the interlayer reflection of the graphitic structure, respectively [29,30]. Compared to that of g-C₃N₄, the peak of p-CN2 shifts slightly from 27.5° to 27.3° and the intensity becomes weaker. It indicates that the interlayer stacking distance of p-CN2 is increased, which is in accordance with the TEM result. In addition, the Fourier transform infrared (FTIR) spectroscopy (Fig. 2b) is further used to confirm that the typical molecular skeletal vibration modes in p-CN samples are close to those in g-C₃N₄. The extra peak at

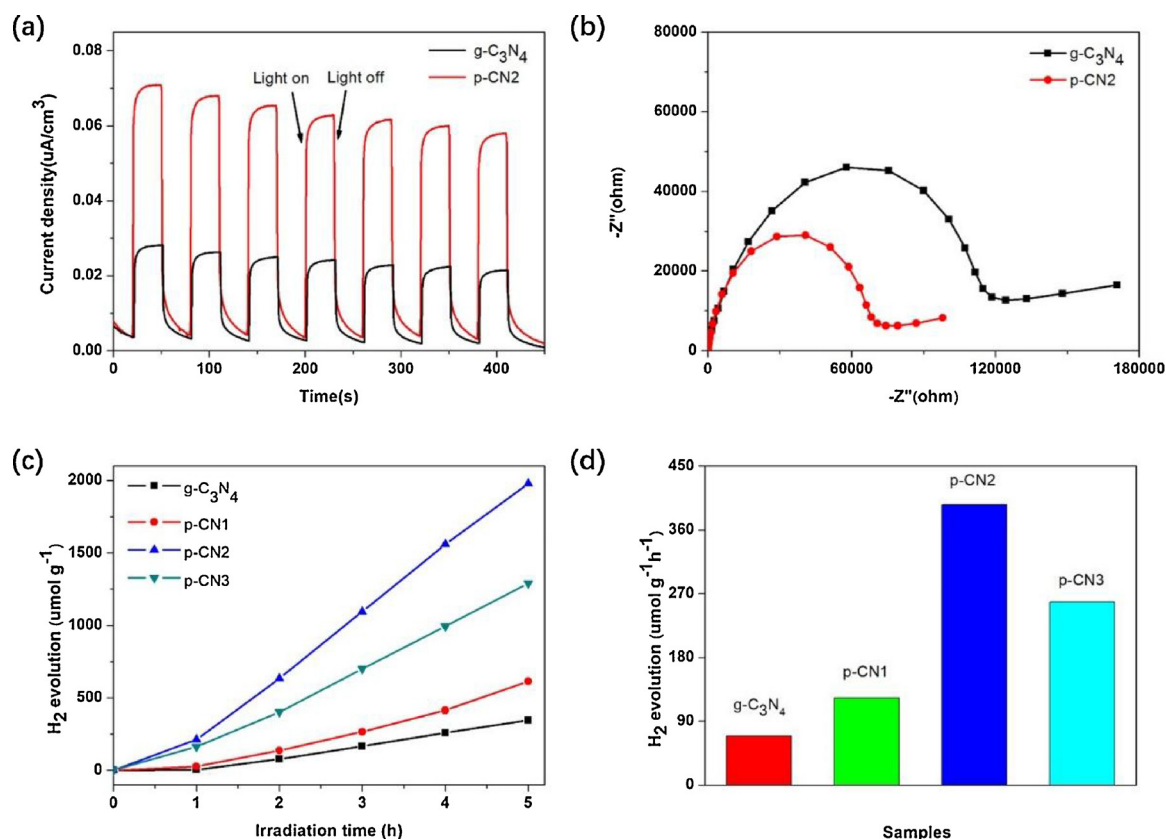


Fig. 5. Transient photocurrent responses under visible light of bulk $g\text{-C}_3\text{N}_4$ and $p\text{-CN2}$ samples. (a). Electrochemical impedance spectra of bulk $g\text{-C}_3\text{N}_4$ and $p\text{-CN2}$ samples (b). Photocatalytic H_2 evolution curves (c), and H_2 evolution rates (d) over bulk $g\text{-C}_3\text{N}_4$, $p\text{-CN1}$, $p\text{-CN2}$ and $p\text{-CN3}$ samples.

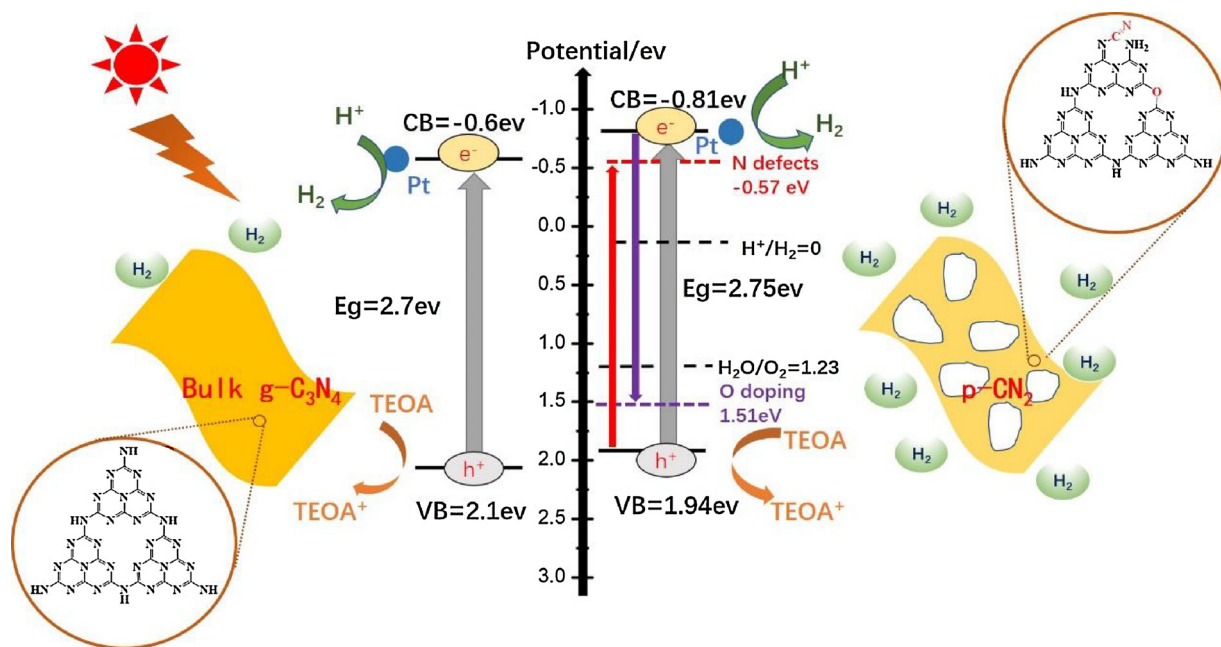


Fig. 6. Possible mechanism for the photocatalytic H_2 production in bulk $g\text{-C}_3\text{N}_4$ and $p\text{-CN2}$, respectively.

2180 cm^{-1} is obviously observed in the $p\text{-CN}$ samples. It is assigned to $\text{C}\equiv\text{N}$ triple bonds, indicating the existence of cyano groups ($\text{C}\equiv\text{N}$) in $p\text{-CN2}$ [31]. It may be ascribed to the suppression of polycondensation after the addition of $(\text{NH}_4)_2\text{S}_2\text{O}_8$. As we know, dicyandiamide is polymerized into melamine at 234°C [6,32] while $(\text{NH}_4)_2\text{S}_2\text{O}_8$ is decomposed to NH_3 (g), SO_2 (g) and O_2 (g) at 120°C , which would act as a role in separating some dicyandiamide crystal grains and

dicyandiamide derived intermediates in space and suppressing the formation of integrated tri-s-triazine structure at 550°C . The sharp peak about 808 cm^{-1} is assigned to typical breathing mode of the triazine units. However, the strong bands in the region from 900 to 1800 cm^{-1} are typical for the melon containing $\text{C}-\text{N}-\text{C}$ heterocycles and are generally associated with skeletal stretching vibrations of aromatic rings, the peaks at $2900\text{--}3600\text{ cm}^{-1}$ can be assigned to adsorbed water

or amine groups [33].

It can also be seen from Fig. 2c and d that all the samples exhibit type IV isotherms with H3 hysteresis loops, which demonstrates the presence of mesoporous structure [34]. For $(\text{NH}_4)_2\text{S}_2\text{O}_8$ modified $\text{g-C}_3\text{N}_4$ samples, the hysteresis loops shift to the region of lower relative pressure and the areas of the hysteresis loops become enlarged, indicating the increase of mesoporosity compared with bulk $\text{g-C}_3\text{N}_4$. As shown in Table S1, the surface area is increased progressively from $11.7 \text{ m}^2 \text{ g}^{-1}$ to $36.9 \text{ m}^2 \text{ g}^{-1}$ with the increased mass of $(\text{NH}_4)_2\text{S}_2\text{O}_8$, which is ascribed to the possible space-occupying effect of undecomposed $(\text{NH}_4)_2\text{S}_2\text{O}_8$. However, when the mass of $(\text{NH}_4)_2\text{S}_2\text{O}_8$ is increased to 0.75 g, the BET surface area and pore volume of the sample (p-CN3) are sharply decreased. This is because the excess undecomposed $(\text{NH}_4)_2\text{S}_2\text{O}_8$ may occupy the generated pores thus decrease the surface area (ca. $19.75 \text{ m}^2 \text{ g}^{-1}$). The change of morphology could also be observed in the TEM images (Fig. S2B). In addition, the wide distributions of BJH pore size in the range of 20–100 nm further confirm the formation of different sized pores. Therefore, the $(\text{NH}_4)_2\text{S}_2\text{O}_8$ plays an important role in facilitating the formation of porous structure during the polycondensation process.

The XPS measurements were carried out to determine the chemical states of the elements for bulk $\text{g-C}_3\text{N}_4$ and p-CN2. Signals of C, N and O elements are displayed in the spectra survey for the two samples (Fig. 3a). As expected, the C1s spectra in Fig. 3b show three main peaks, which could be assigned to adventitious carbon species (284.6 eV), C–NH_x ($x = 1, 2$) on the edges of heptazine units (286.2 eV) and N–C≡N coordination in the framework of $\text{g-C}_3\text{N}_4$ (288.0 eV), respectively [21]. Meanwhile, as shown in Fig. 3c, the N 1s XPS spectra for the samples contain three components at 398.7, 400.1, and 401.1 eV, corresponding to sp^2 bonded N in the tri-s-triazine ($\text{N}_{2\text{C}}$), bridging nitrogen atoms in N–(C)₃ and NH_x groups in the heptazine framework, respectively. Additionally, the very weak peak at 404.2 eV was attributed to the charging effects or positive charge localization in the heterocycles [35]. The O 1s spectra (Fig. 3d) of the two samples were fitted into two peaks at 533.1 and 531.8 eV, which were ascribed to the adsorbed water and CO_2 , respectively [25,36]. In comparison with the $\text{g-C}_3\text{N}_4$, the binding energies of C 1s, N 1s and O 1s spectra in p-CN2 show a little bit of variations. In C 1s spectrum, the intensity of the peak located at 284.6 eV increases, indicating the loss of lattice nitrogen and the formation of nitrogen vacancy in p-CN2 [16], and the peak at 286.2 eV is more intensified compared to the same feature for $\text{g-C}_3\text{N}_4$ (Fig. 3b, bottom), which can be taken as additional evidence for the existence of cyano groups (as seen by FTIR) since C≡N groups possess similar C 1s binding energies to C–NH_x [37]. Surprisingly, a new peak at 288.7 eV is observed in p-CN2, which may be attributed to the C atoms bonded with O (C–O) [26,27]. In the N 1s spectrum, the $\text{N}_{3\text{C}}$ and $\text{N}_{2\text{C}}$ peaks in p-CN2 exhibit a small shift to lower binding energy, which could be ascribed to the existence of cyano groups whose N 1s binding energy are intermediate between those of $\text{N}_{2\text{C}}$ and $\text{N}_{3\text{C}}$. Furthermore, the ratio of $\text{N-sp}^2/\text{N-sp}^3$ increases from 1.91 for pristine $\text{g-C}_3\text{N}_4$ to 3.71 for p-CN2 in Table S2, implying the existence of cyano groups on the $\text{N}_{2\text{C}}$ lattice sites in p-CN2. To further confirm the introduction of surface N defects, the element contents in the two samples are further compared by elemental analysis (Fig. S3). The atomic ratios of carbon to nitrogen agree almost 0.66 for bulk $\text{g-C}_3\text{N}_4$, lower than 0.70 for the p-CN2, while the surface atomic ratio from XPS reveals that the C/N molar ratio of pristine $\text{g-C}_3\text{N}_4$ (0.85) is also lower than that of p-CN2 (0.89) (Table S3), indicating the nitrogen vacancy exists in the p-CN2 nanosheets. For O 1s spectrum, a new peak at the low binding energy of 530.7 eV appears in p-CN2 sample, which may be assigned to C–O and N–C–O species in lattices [38]. Although both the C 1s peak and O 1s peak demonstrate that C–O bond may be generated in p-CN2, it still needs to be confirmed further. Besides, no signals belonging to sulfur species can be found in p-CN2 (Fig. S4), indicating that the sulfur atom may be released as gaseous form and has not been incorporated into the lattice of $\text{g-C}_3\text{N}_4$ during heating treatment.

To confirm the existence of the nitrogen defects and oxygen dopants in p-CN2 sample, room-temperature electron paramagnetic resonance (EPR) spectra were recorded. In Fig. 3e both bulk $\text{g-C}_3\text{N}_4$ and p-CN2 exhibit a paramagnetic absorption signal with the g value of 2.0034, which can be assigned to the unpaired electrons on sp^2 -carbon atoms within the π -conjugated aromatic rings. Compared with that in bulk $\text{g-C}_3\text{N}_4$, this EPR signal in p-CN2 is much declined, which can be ascribed to the substitution of O to N forming covalent bonds with C, reducing the number of unpaired electrons and decreasing the EPR signal. In addition, the shoulder peak appears at $g = 1.9884$, probably because of the substitution of the N atom in the heptazine unit with an O atom creates one unpaired spin [27]. The g value is different from that in the reference, and it may be ascribed to the different substitution sites of nitrogen atoms. On the basis of the characterization results, the possible chemical structure of p-CN2 is proposed in Fig. 3f.

3.2. Optical and electronic properties of the photocatalysts

To investigate the band structure and photo absorption ability, the UV–vis DRS spectra were carried out and showed in the Fig. 4a. It is obvious to see that the absorption edges in p-CN2 show a remarkable blue-shift in comparison with the bulk $\text{g-C}_3\text{N}_4$, which is consistent with the color variation from yellow bulk $\text{g-C}_3\text{N}_4$ to light yellow p-CN2 (insets in Fig. 4a). The bandgap energies of all samples are derived by Kubelka–Munk method [12]. Fig. 4b shows the bandgap of p-CN2 (2.75 eV) is a little larger than that of $\text{g-C}_3\text{N}_4$ (2.7 eV), which may be ascribed to the quantum confinement effect (QCE) induced by the decline in thickness of p-CN2. In addition, an optical absorption tail could be found in p-CN2, hinting that defect state or dopant level may be generated. Thus, new generated energy levels are also derived from UV–vis spectrum of p-CN2, known as defect states. From valence band (VB) XPS spectra, the positions of VB maxima are estimated to be 2.1 eV and 1.94 eV for pristine $\text{g-C}_3\text{N}_4$ and p-CN2, respectively (Fig. S6). The diagram of band structure will be shown later.

As shown in Fig. 4c, when the samples were excited by 325 nm laser, a broad PL emission peak at ca. 470 nm appeared. An obvious red-shift of the emission peak from 480 to 508 nm can be found for bulk $\text{g-C}_3\text{N}_4$ to p-CN2, which may contradict to the UV analysis. In fact, it confirms the formation of defect states. Besides, the shape of emission peak is changed obviously, suggesting that the electron transition path is also changed. As we know, the electronic band states of $\text{g-C}_3\text{N}_4$ are composed of the δ band (sp^3 C–N bonding), π band (sp^2 C–N bonding), and lone pair (LP) state of the bridge nitride atom. In order to figure out the band structure and electron transition, the PL spectrum of p-CN2 is fitted by three Gaussian peaks, which are exhibited at 440–460 nm (peak A), 490–510 nm (peak B), and 530–560 nm (peak C), as shown in Fig. 4d. The luminescence emission peak A reflects the intrinsic radiative emission of the charge transition from the highest occupied molecular orbital (HOMO) which comprises 2p orbitals of low coordinated N atoms, to the lowest unoccupied molecular orbital (LUMO), which mainly consists of the C 2p character. The intensity of peak A drops sharply after modification of $(\text{NH}_4)_2\text{S}_2\text{O}_8$, suggesting the intrinsic radiative recombination is suppressed. The emission peaks B and C correspond to the transitions between antibonding π^* -LP and antibonding π^* - π , respectively. The ratios of these two peaks increase in p-CN2, suggesting that the corresponding electron transitions become pre-dominant [39]. It may be ascribed to the increased amount of sp^2 C–N bonding, which is induced by the formation of nitrogen vacancy. In addition, oxygen atom preferentially occupies the site of bridge nitrogen atom, therefore the LP state is also affected. Thus, nitrogen vacancy and oxygen dopant have effects on the band structure of $\text{g-C}_3\text{N}_4$ because of the variation on the number of sp^2 C–N bonds and bridge nitrogen atoms, leading to the change of electron transition and suppression of charge recombination.

Photoelectrochemical measurements including transient photocurrent under visible light and electrochemical impedance spectra (EIS)

irradiation were performed to further study the separation and transportation of photogenerated carriers. It could be seen in Fig. 5a that both pristine g-C₃N₄ and p-CN2 electrodes show obvious positive photocurrents by several on–off cycles of visible-light irradiation at an applied potential of -0.2 V (vs. Ag/AgCl, pH 6.9) [40]. Additionally, p-CN2 shows larger photocurrent density than the bulk g-C₃N₄ electrode, indicating that the charge separation in p-CN2 is more efficient than that in pristine g-C₃N₄. Besides, it is obvious in Fig. 5b that the diameter of the semicircular Nyquist curve of p-CN2 is smaller than that of bulk g-C₃N₄, implying that the resistance at the solid/electrolyte interface is significantly decreased. It is benefit to charge transfer, which also suggests that the efficiency of charge separation is much higher in p-CN2.

3.3. Photocatalytic performance

The photocatalytic performance of bulk g-C₃N₄ and p-CN samples was evaluated by a typical time course of hydrogen production under visible light irradiation ($\lambda > 420$ nm) with 3 wt% Pt as co-catalyst at room temperature. As presented in Fig. 5c, all the p-CN samples show largely enhanced H₂ evolution activity. The H₂ evolution rate for both p-CN1 ($122.84 \mu\text{mol h}^{-1} \text{g}^{-1}$) and p-CN3 ($258.18 \mu\text{mol h}^{-1} \text{g}^{-1}$) are higher than that of the bulk g-C₃N₄ ($69.25 \mu\text{mol h}^{-1} \text{g}^{-1}$). Among all the p-CN samples, p-CN2 displays the best photocatalytic performance with the H₂ evolution rate reaching $395.96 \mu\text{mol h}^{-1} \text{g}^{-1}$, which is approximately 6 times higher than that of bulk g-C₃N₄ (Fig. 5d). The results directly certify the positive effects of the (NH₄)₂S₂O₈ on promoting the photocatalytic activity of g-C₃N₄. To explore the details of visible light driven activity for hydrogen evolution, the apparent quantum yield (AQY) was estimated at different wavelengths, as shown in Fig. S7. The AQY for p-CN2 was calculated to be 0.79% at $\lambda = 420$ nm (Fig. S7), and p-CN2 shows consistently higher AQY than pristine g-C₃N₄ at all wavelengths above 420 nm. In comparison, the g-C₃N₄ only shows activity at irradiation wavelengths below 450 nm, implying that more photons in p-CN2 can attend hydrogen evolution reaction. Besides, the stability test in Fig. S8 shows the photocatalytic H₂ production activity of p-CN2 is well retained after four successive cycles while the phase structures are not changed (Fig. S9), suggesting the high stability and durability of the catalyst.

Based on the above characterization, the band structure is illustrated in Fig. S10. Combined with the bandgap from UV–vis DRS, the CB edges of bulk g-C₃N₄ and p-CN2 are estimated to be -0.6 eV and -0.81 eV, respectively (Fig. 6). In addition, the upshift of CB edge in p-CN2 is also evidenced by using Mott–Schottky plots (Fig. S11). Obviously, the potential of conduction band in p-CN2 is more negative than that of g-C₃N₄, implying that p-CN2 possesses stronger photocatalytic reductive ability [41]. As mentioned above, the higher specific surface area of p-CN2 sample with porous structure is favorable for exposing more active sites to adsorb H⁺ and promoting mass transfer. The bandgap of p-CN2 is a little larger than that of pristine g-C₃N₄, which is confirmed by UV–vis DRS. However, the nitrogen defects and oxygen dopants introduce intraband states into the band gap of p-CN2, resulting in a lower excitation energy of excitons and a shorter migration path of the photo-generated electrons. The transitions from different impurity levels suppress the recombination of charge carriers. Thus, the porous oxygen doped g-C₃N₄ with nitrogen defects shows excellent photocatalytic hydrogen evolution activity, which is mainly ascribed to the synergetic effect between the nitrogen defects and oxygen dopants that promotes charge separation, and the increased surface area that provides more reaction sites for hydrogen production.

4. Conclusions

In summary, nitrogen defects and oxygen dopants have been successfully introduced into thin and porous g-C₃N₄ nanosheets by a facile method via polymerizing dicyandiamide and (NH₄)₂S₂O₈. Compared

with bulk g-C₃N₄, the modified sample (p-CN2) exhibits an excellent photocatalytic hydrogen evolution activity with the rate up to $395.96 \mu\text{mol h}^{-1} \text{g}^{-1}$, which is almost 6 times higher than that of pristine g-C₃N₄. The enhancement of photocatalytic activity is attributed to the increase in surface area and improved charge separation, which is induced by the synergetic effect between the nitrogen defects and oxygen dopants. The introduction of nitrogen defects and oxygen dopant leads to the change of π band state and LP state, which gives rise to the change of electron transition. Because the transitions from impurity levels play a predominant role in excitation process, the charge recombination is thus suppressed. In addition, it is found that (NH₄)₂S₂O₈ plays multi-function roles in the co-pyrolysis process. It not only restrains polycondensation to generate nitrogen defects but also introduces porous structure and oxygen dopants due to its strong oxidative ability. Thus, this work provides a different method to design highly efficient photocatalysts by affecting electron transition. It is worth noting that the present work can deepen our understanding on the complex excitation process in photocatalytic reaction and inspire us to improve the activity further by changing the band state of g-C₃N₄.

Acknowledgements

This work was financially supported by Southern University of Science and Technology (SUSTech) start fund through Shenzhen Peacock Talent program, Basic Research Fund of Shenzhen (JCYJ20150507170334573), and Guangdong Innovative and Entrepreneurial Research Team Program (No. 2016ZT06N532). Z.L. also thanks the support from the National Natural Science Foundation of China (21703097). This work was also supported by the Pico Center at SUSTech that receives support from Presidential fund and Development and Reform Commission of Shenzhen Municipality.

Appendix A. Supplementary data

Supplementary material related to this article can be found, in the online version, at doi:<https://doi.org/10.1016/j.apcatb.2018.08.059>.

References

- [1] X. Wang, K. Maeda, A. Thomas, T.K. Takanabe, G. Xin, J.M. Carlsson, K. Domen, M. Antonietti, A metal-free polymeric photocatalyst for hydrogen production from water under visible light, *Nat. Mater.* 8 (2009) 76–80.
- [2] Y. Wang, J. Zhang, X. Wang, M. Antonietti, H. Li, Boron- and fluorine-containing mesoporous carbon nitride polymers: metal-free catalysts for cyclohexane oxidation, *Angew. Chem.* 49 (2010) 3356–3359.
- [3] G. Dong, L. Zhang, Porous structure dependent photoreactivity of graphitic carbon nitride under visible light, *J. Mater. Chem.* 22 (2011) 1160–1166.
- [4] X. Chen, J. Zhang, X. Fu, M. Antonietti, X. Wang, Fe-g-C₃N₄-catalyzed oxidation of benzene to phenol using hydrogen peroxide and visible light, *J. Am. Chem. Soc.* 131 (2009) 11658–11659.
- [5] X. Zhang, X. Xie, H. Wang, J. Zhang, B. Pan, Y. Xie, Enhanced photoresponsive ultrathin graphitic-phase C₃N₄ nanosheets for bioimaging, *J. Am. Chem. Soc.* 135 (2013) 18–21.
- [6] W.J. Ong, L.L. Tan, Y.H. Ng, S.T. Yong, S.P. Chai, Graphitic carbon nitride (g-C₃N₄)-based photocatalysts for artificial photosynthesis and environmental remediation: are we a step closer to achieving sustainability? *Chem. Rev.* 116 (2016) 7159–7329.
- [7] L. Shi, T. Wang, H. Zhang, K. Chang, J. Ye, Electrostatic self-assembly of nanosized carbon nitride nanosheet onto a zirconium metal-organic framework for enhanced photocatalytic CO₂ reduction, *Adv. Funct. Mater.* 25 (2015) 5360–5367.
- [8] Y. Wang, H. Li, J. Yao, X. Wang, M. Antonietti, Synthesis of boron doped polymeric carbon nitride solids and their use as metal-free catalysts for aliphatic C–H bond oxidation, *Chem. Sci.* 2 (2011) 446–450.
- [9] Z. Zhang, D. Jiang, D. Li, M. He, M. Chen, Construction of SnNb₂O₆ nanosheet/g-C₃N₄ nanosheet two-dimensional heterostructures with improved photocatalytic activity: synergetic effect and mechanism insight, *Appl. Catal. B: Environ.* 183 (2016) 113–123.
- [10] F.K. Kessler, Y. Zheng, D. Schwarz, C. Merschjann, W. Schnick, X. Wang, M.J. Bojdys, Functional carbon nitride materials—design strategies for electrochemical devices, *Nat. Rev. Mater.* 2 (2017).
- [11] Y. Hou, Z. Wen, S. Cui, X. Guo, J. Chen, Constructing 2D porous graphitic C₃N₄ nanosheets/nitrogen-doped graphene/layered MoS₂ ternary nanojunction with enhanced photoelectrochemical activity, *Adv. Mater.* 25 (2013) 6291–6297.
- [12] R.J. Ran, T.Y. Ma, G. Gao, X. Du, S. Qiao, Porous P-doped graphitic carbon nitride nanosheets for synergistically enhanced visible-light photocatalytic H₂ production,

- Energy Environ. Sci. 8 (2015) 3708–3717.
- [13] S. Fang, Y. Xia, K. Lv, Q. Li, J. Sun, M. Li, Effect of carbon-dots modification on the structure and photocatalytic activity of g-C₃N₄, *Appl. Catal. B: Environ.* 185 (2016) 225–232.
- [14] S. Samanta, S. Martha, K. Parida, Facile synthesis of Au/g-C₃N₄ nanocomposites: an inorganic/organic hybrid plasmonic photocatalyst with enhanced hydrogen gas evolution under visible-light irradiation, *ChemCatChem* 6 (2014) 1453–1462.
- [15] Z.A. Huang, Q. Sun, K. Lv, Z. Zhang, M. Li, B. Li, Effect of contact interface between TiO₂ and g-C₃N₄ on the photoreactivity of g-C₃N₄/TiO₂ photocatalyst: (0 0 1) vs (1 0 1) facets of TiO₂, *Appl. Catal. B: Environ.* 164 (2015) 420–427.
- [16] Q. Han, B. Wang, Y. Zhao, C. Hu, L. Qu, A graphitic-C₃N₄ “Seaweed” architecture for enhanced hydrogen evolution, *Angew. Chem. Int. Ed.* 54 (39) (2015) 11433–11437.
- [17] Y. Yin, A.P. Alivisatos, Formation of hollow nanocrystals through the nanoscale Kirkendall effect, *Science* 304 (2004) 711–714.
- [18] T. Wang, X. Meng, P. Li, S. Ouyang, K. Chang, G. Liu, Z. Mei, J. Ye, Photoreduction of CO₂ over the well-crystallized ordered mesoporous TiO₂ with the confined space effect, *Nano Energy* 9 (2014) 50–60.
- [19] P. Niu, G. Liu, H.M. Cheng, Nitrogen vacancy-promoted photocatalytic activity of graphitic carbon nitride, *J. Phys. Chem. C* 116 (2012) 11013–11018.
- [20] D. Zhang, Y. Guo, Z. Zhao, Porous defect-modified graphitic carbon nitride via a facile one-step approach with significantly enhanced photocatalytic hydrogen evolution under visible light irradiation, *Appl. Catal. B: Environ.* 226 (2018) 1–9.
- [21] H. Yu, R. Shi, Y. Zhao, T. Bian, Y. Zhao, C. Zhou, G.I. Waterhouse, L.Z. Wu, C.H. Tung, T. Zhang, Alkali-assisted synthesis of nitrogen deficient graphitic carbon nitride with tunable band structures for efficient visible-light-driven hydrogen evolution, *Adv. Mater.* 29 (2017) 1605148.
- [22] X. She, L. Liang, H. Ji, M. Zhao, Y. Li, L. Huang, D. Du, X. Hui, H. Li, Template-free synthesis of 2D porous ultrathin nonmetal-doped g-C₃N₄ nanosheets with highly efficient photocatalytic H₂ evolution from water under visible light, *Appl. Catal. B: Environ.* 187 (2016) 144–153.
- [23] F. He, G. Chen, Y. Yu, Y. Zhou, Y. Zheng, S. Hao, Sulfur-bubble template-mediated synthesis of uniform porous g-C₃N₄ with superior photocatalytic performance, *Chem. Commun.* 51 (2015) 425–427.
- [24] D.H. Lan, H.T. Wang, L. Chen, C.T. Au, S.F. Yin, Phosphorous-modified bulk graphitic carbon nitride: facile preparation and application as an acid-base bifunctional and efficient catalyst for CO₂ cycloaddition with epoxides, *Carbon* 100 (2016) 81–89.
- [25] J. Li, B. Shen, Z. Hong, B. Lin, B. Gao, Y. Chen, A facile approach to synthesize novel oxygen-doped g-C₃N₄ with superior visible-light photoreactivity, *Chem. Commun.* 48 (2012) 12017–12019.
- [26] Z.F. Huang, J. Song, L. Pan, Z. Wang, X. Zhang, J.J. Zou, W. Mi, X. Zhang, L. Wang, Carbon nitride with simultaneous porous network and O-doping for efficient solar-energy-driven hydrogen evolution, *Nano Energy* 12 (2015) 646–656.
- [27] P. Qiu, C. Xu, H. Chen, F. Jiang, X. Wang, R. Lu, X. Zhang, One step synthesis of oxygen doped porous graphitic carbon nitride with remarkable improvement of photo-oxidation activity: role of oxygen on visible light photocatalytic activity, *Appl. Catal. B: Environ.* 206 (2017) 319–327.
- [28] T.R. Chetia, M.S. Ansari, M. Qureshi, Graphitic carbon nitride as a photovoltaic booster in quantum dot sensitized solar cells: a synergistic approach for enhanced charge separation and injection, *J. Mater. Chem. A* 4 (2016) 5528–5541.
- [29] A. Thomas, A. Fischer, F. Goettmann, M. Antonietti, J.O. Mueller, R. Schloegl, J.M. Carlsson, ChemInform abstract: graphitic carbon nitride materials: variation of structure and morphology and their use as metal-free catalysts, *ChemInform* 40 (2009) 4893–4908.
- [30] M. Arslan, A.H. Duymuş, F. Yakuphanoglu, Optical properties of the poly(N-benzylaniline) thin film, *J. Phys. Chem. B* 110 (2006) 276.
- [31] C. Liu, H. Huang, W. Cui, F. Dong, Y. Zhang, Band structure engineering and efficient charge transport in oxygen substituted g-C₃N₄ for superior photocatalytic hydrogen evolution, *Appl. Catal. B: Environ.* 230 (2018) 115–124.
- [32] J. Zhang, G. Zhang, X. Chen, S. Lin, L. Mohlmann, G. Dolega, G. Lipner, M. Antonietti, S. Blechert, X. Wang, Co-monomer control of carbon nitride semiconductors to optimize hydrogen evolution with visible light, *Angew. Chem. Int. Ed. Engl.* 51 (2012) 3183–3187.
- [33] L. Zeng, X. Ding, Z. Sun, W. Hua, W. Song, S. Liu, L. Huang, Enhancement of photocatalytic hydrogen evolution activity of g-C₃N₄ induced by structural distortion via post-fluorination treatment, *Appl. Catal. B: Environ.* 227 (2018) 276–284.
- [34] J. Qin, S. Wang, H. Ren, Y. Hou, X. Wang, Photocatalytic reduction of CO₂ by graphitic carbon nitride polymers derived from urea and barbituric acid, *Appl. Catal. B: Environ.* 179 (2015) 1–8.
- [35] B. Long, J. Lin, X. Wang, Thermally-induced desulfurization and conversion of guanidine thiocyanate into graphitic carbon nitride catalysts for hydrogen photosynthesis, *J. Mater. Chem. A* 2 (2014) 2942–2951.
- [36] L. Ming, H. Yue, L. Xu, F. Chen, Hydrothermal synthesis of oxidized g-C₃N₄ and its regulation of photocatalytic activity, *J. Mater. Chem.* 2 (2014) 19145–19149.
- [37] H. Gao, S. Yan, J. Wang, Y.A. Huang, P. Wang, Z. Li, Z. Zou, Towards efficient solar hydrogen production by intercalated carbon nitride photocatalyst, *Phys. Chem. Chem. Phys.* 15 (2013) 18077–18084.
- [38] A. Sanchezsanchez, F. Suarezgarcia, A. Martinezalonso, J.M.D. Tascon, Aromatic polyamides as new precursors of nitrogen and oxygen-doped ordered mesoporous carbons, *Carbon* 70 (2014) 119–129.
- [39] C. Hu, W.-Z. Hung, M.-S. Wang, P.-J. Lu, Phosphorus and sulfur codoped g-C₃N₄ as an efficient metal-free photocatalyst, *Carbon* 127 (2018) 374–383.
- [40] L.J. Fang, Y.H. Li, P.F. Liu, D.P. Wang, H. Zeng, X. Wang, H.G. Yang, Facile fabrication of large-aspect-ratio g-C₃N₄ nanosheets for enhanced photocatalytic hydrogen evolution, *ACS Sustain. Chem. Eng.* 5 (2017).
- [41] P. Yang, H. Ou, Y. Fang, X. Wang, A facile steam reforming strategy to delaminate layered carbon nitride semiconductors for photoredox catalysis, *Angew. Chem. Int. Ed. Engl.* 56 (2017) 3992–3996.